Journal of Power Sources 195 (2010) 6924–6936

Contents lists available at ScienceDirect

Journal of Power Sources

journal homepage: www.elsevier.com/locate/jpowsour

Effect of minor nickel alloying with zinc on the electrochemical and corrosion behavior of zinc in alkaline solution

Abdel-Rahman El-Sayed*, Hossnia S. Mohran, Hany M. Abd El-Lateef

Chemistry Dept., Faculty of Science, Sohag University, Sohag 82524, Egypt

ARTICLE INFO

Article history:
Received 7 December 2009
Received in revised form 27 February 2010
Accepted 14 March 2010
Available online 1 April 2010

Keywords:
Electrochemical behavior
Corrosion
Zinc
Minor Ni alloying
Alkaline solution

ABSTRACT

The electrochemical and corrosion behavior of pure zinc and Zn–0.5Ni alloy in strong alkaline solution (7 M KOH) was investigated by Tafel plot, potentiodynamic, potentiostatic and electrochemical impedance spectroscopy (EIS) methods, and characterized by X-ray diffraction (XRD) and scanning electron microscope (SEM). Measurements were conducted under different experimental conditions. The results of both Tafel plot extrapolation and the electrochemical impedance spectroscopy (EIS) measurements exhibited the same trend, which the cathodic and anodic processes on the alloy surface are less significant compared with those on the pure zinc. The results revealed that, the shift in steady state of open-circuit potential (E_{corr}) to more negative potential in the case of the studied alloy compared with that of pure zinc has a positive effect on both charge efficiency and self-discharge.

The anodic potentiodynamic measurements demonstrated that the polarization curves exhibited active/passive transition. The active dissolution of both pure zinc and its alloy increases with increasing temperature and scan rate. The activation energy (E_a) value of active region and peak current (I_{Al}) of the two studied electrodes in the investigated alkaline solution is calculated and compared. In the case of alloy, the results obtained at certain positive potential (+425 mV vs. SCE), exhibited high current density indicating that the most passive layer was destroyed. This indicates that the addition of small amount from Ni to Zn promotes the electrochemical reaction (in the passive region), acting as so-called self catalysis. Accordingly, one can conclude that, the electrochemical behavior of the investigated alloy in strong alkaline solution contributes to suppression of hydrogen gas evolution and increases the corrosion resistance. In addition, reactivation of the alloy surface takes place in the passive region.

1. Introduction

Zinc is widely used as a negative active material for batteries (e.g., Leclanchè batteries and alkaline manganese batteries) because it has a large energy capacity and economic advantages. Zinc has been added with mercury to suppress the evolution of hydrogen gas brought on by the self-discharge reactions of zinc and by the increase in internal cell impedance [1–14]. The use of mercury has become an environmental issue and the attention has been focused on developing mercury-free batteries. McLarnon et al. [15,16] have addressed the status of research and development of both primary and secondary alkaline zinc batteries. In general, either zinc or its alloys are used as anodes in these batteries. The purity of the zinc is very high, i.e., of the order of 99.9 wt.% or more. In some cells, zinc is alloyed with cadmium, mercury, lead, etc. Cadmium and mercury are highly undesirable from the point of view of pollution. In particular, the presence of mercury in alkaline Zn–MnO_2 dry cells is considered to be a potential source of pollution, since the production of alkaline MnO_2 cells is continuously increasing. Most probably, the traditional Leclanchè system may be abandoned completely, since the alkaline system possesses much better electrochemical characteristics. Hence, the development of zinc or zinc-based alloys as anodes for alkaline power sources has become a necessity and in this connection, development of mercury-free zinc assumes great importance. Similarly, Zn-air battery technology also requires mercury-free zinc anodes.

As it is known that, Zn corrosion in alkaline solution is cathodic controlled, so the rate of the cathodic hydrogen evolution limits the Zn corrosion rate. Hence the best way to slow down the corrosion process is to reduce the hydrogen evolution rate, which can be achieved by the introduction of a small amount of other metals as Bi, Pb, Al and In into Zn [17].

Despite numerous publications on zinc and its alloys in alkaline solutions [9–12,18–24], there is not any information in the literature on synthetic Zn–Ni alloy in any aqueous solution.

* Corresponding author. Tel.: +20 934601159; fax: +20 934601159.
E-mail address: elsayed777@yahoo.com (A.-R. El-Sayed).

0378-7753/$ – see front matter © 2010 Elsevier B.V. All rights reserved.
doi:10.1016/j.jpowsour.2010.03.071

The important criteria for a good battery anode are as follows [18]:

i. High negative open-circuit potential (OCP) in the media under investigation;
ii. Zero, or negligible, corrosion rate;
iii. Minimum polarization;
iv. Very high utilization efficiency;
v. Environmentally safe manufacturing processes for both the anode and the electrolyte, as well as for the batteries themselves, and
vi. Highly competitive cost of battery production.

To achieve the above characteristics, a new alloy based on high-purity zinc with small amount of Ni has been cast and characterized as anodes in alkaline solution.

The aim of this paper is to get more knowledge about the electrochemical and corrosion behavior of Zn–Ni alloy. In this sense, the corrosion behavior of the synthetic Zn–Ni alloy, prepared in our laboratory is compared with that of pure zinc in 7 M KOH solution. Tafel polarization, potentiodynamic, potentiostatic, and the electrochemical impedance spectroscopy "EIS" techniques were used. Also the purpose of the present work is to throw more light on the specific role of Ni as a minor element on the corrosion of Zn electrode. The characterization of microstructural and the composition of the passive layer formed on the surfaces of both Zn and Zn–Ni alloy under anodic polarization were performed using scanning electron microscope (SEM) and X-ray diffraction (XRD).

2. Experimental

2.1. Materials and solutions

7 M solution of KOH (analytical grade) was prepared by dissolving the appropriate weight in doubly distilled water. Zn and Ni of high purity (99.999%; Johnson Matthey Chemicals Ltd.) were used to prepare Zn–Ni alloy as disk electrodes ($A = 0.196\,cm^2$) in a Gallenkamp muffle furnace using evacuated closed silica tubes at 1000 °C for 24 h. The melts were shaken every 6 h to ensure the homogeneity of melting alloys and finally the melts were quenched in an ice as previously discussed [25]. One Zn–Ni alloy was prepared with the composition of 99.5% Zn–0.5% Ni alloy.

The prepared alloy was analyzed using X-ray photoelectron spectroscopy. For the alloy, the percentage of Zn and Ni was found in accord with the percentage of mixing Zn and Ni. The microhardness of Zn and prepared Zn–Ni alloy was measured using a Leiz Wetzlar Microhardness tester with a Vickers diamond pyramid indicator; a load of 100 g was used, and the microhardness was expressed in kilograms per square millimeter.

2.2. Electrochemical measurements

The measurements were performed on planar disk electrode embedded in an Araldite holder. Prior to each measurement the electrodes were polished with sequacious grades of emery paper, degreased in pure ethanol and washed in running bidistilled water before being inserted in the polarization cell. The reference electrode was a saturated calomel electrode (SCE) to which all potentials are referred.

The cell description is given elsewhere [26]. To remove any surface contamination and air formed oxide, the working electrode was kept at −1500 mV (SCE) for 5 min in the tested solution, disconnected shaken free of adsorbed hydrogen bubbles and then cathodic and anodic polarization was recorded. Potentiostat/galvanostat (EG&G Model 273) connected with a personal computer (IBM Model 30) was used for the measurements.

2.2.1. Tafel polarization technique

The extrapolation of cathodic and anodic Tafel lines was carried out in a potential range ±200 mV with respect to corrosion potential (E_{corr}) at scan rate of 1 mV s^{-1} using software version 342C supplied from EG&G Princeton Applied Research.

2.2.2. Potentiodynamic technique

The potentiodynamic polarization studies were carried out with electrodes having a surface area of 0.196 cm^2. The potential was altered automatically from the steady state open-circuit potential (E_{corr}) up to +1500 mV (SCE) and at different scan rates using software version 342C supplied from EG&G Princeton Applied Research.

2.2.3. Potentiostatic technique

The anodic potential was fixed at a required constant value and the variation of current density was recorded as a function of time (current density – time transients).

2.2.4. Electrochemical impedance spectroscopy (EIS)

Electrochemical impedance spectroscopy (EIS) measurements were performed with a phase-sensitive detector (amplifier) (Model 5208) driven by a potentiostat/galvanostat apparatus (model 273) from EG&G Instruments. The electrochemical software of this Model is 378. The EIS were acquired at different applied potentials (0 and ±100 mV vs. E_{ocp}) in the frequency range from 100 kHz to 5 mHz. An amplitude of 5 mV peak to peak was used for the ac signal for all EIS measurements.

2.3. Surface characterization

X-ray diffraction of the prepared alloy was carried out using a diffractometer with an iron filter and copper radiation was used with an accelerating voltage of 30 kV and a filament current of 20 mA. The morphology of both Zn and Ni oxides was examined using scanning electron microscope (JEOL, model 5300).

Each experiment was performed with freshly prepared solution and clean set of electrodes. Measurements were conducted at 25, 35, 45 and 55 ± 0.5 °C for each investigated electrode. For this purpose ultrathermostat model Frigiter 6000 382 (SELECTA) was used.

3. Results and discussion

3.1. Mechanical properties and composition of Zn, Zn–Ni alloy

3.1.1. Microhardness measurements

The hardness values of Zn and Zn–0.5Ni alloy were measured by employing the Vickers microhardness test procedure with a Vickers pyramidal indentor and a load of 100 g. The data reveal that the microhardness in the case of Zn–0.5Ni alloy (72.2 ± 0.5 HV) is higher than that of pure Zn (38.1 ± 0.2 HV). The increase in microhardness can be explained on the basis that the addition of Ni to Zn can result in the formation of intermetallic compounds in the solid state [27]. Intermetallic compounds are generally brittle and hard [28]. The bonding character of Zn–Ni alloys can be assumed as to be mainly metallic. Accordingly, the existence of Ni in certain percent in Zn alloy would lead to the improvement of mechanical properties of Zn. According to Alfantazi and Erb [29] the hardness effects are due to the formation of different phases. Therefore, the formation of γ-Zn_3Ni (confirmed by XRD) has an influence on the hardness of Zn–0.5Ni alloy.

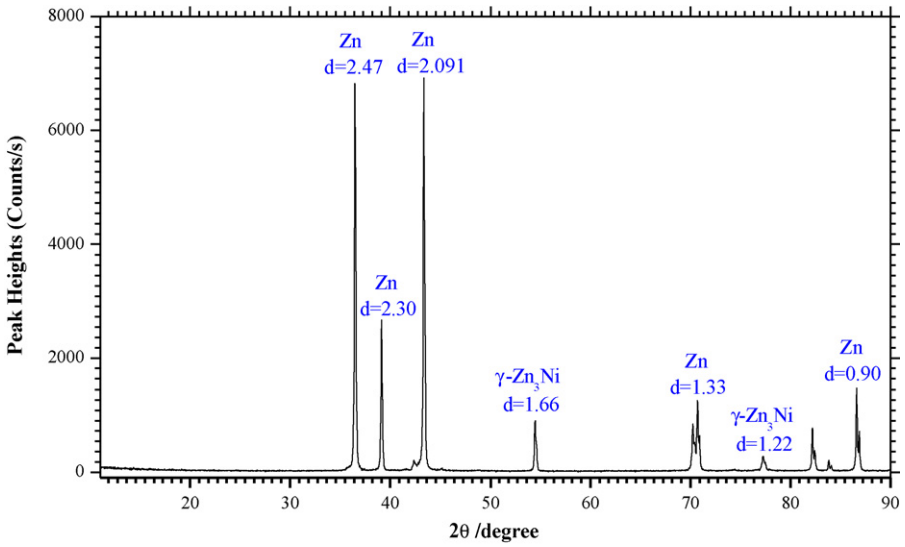

Fig. 1. X-ray diffraction pattern on the surface of prepared Zn–0.5Ni alloy.

3.1.2. X-ray diffraction

The data given in Fig. 1 show X-ray diffraction of Zn–Ni alloys I (0.5% Ni) prepared by the usual melt-quench technique which consists of a Zn–Ni intermetallic structure with the same ratio of the mixture. However, some separated Zn and Ni in their elemental phases can exist together with Zn–Ni matrix in the alloy (γ-Zn_3Ni).

3.1.3. SEM photographs

Scanning electron microscope is a good tool to investigate the surface morphology of the materials. In our work it has been used to determine the change in surface morphology occurred in the prepared samples due to the alloying of Zn and Ni elements under the conditions described previously. In Fig. 2, SEM micrographs for samples of (a) pure Zn, (b) Zn–0.5Ni alloy. Fig. 2a shows typical SEM micrograph of pure Zn. As seen the surface has silvery grey colour and characterized with longitudinal scratches on the surface. These longitudes are perturbed as due to the presence of 0.5% of Ni element incorporated in Zn (Fig. 2b). Furthermore, the depth of the scratches becomes lower. The variety in colours on the micrographs indicates that the investigated sample is with multi-phase nature. On the other hand the irregularity of colours distribution may emphasize the heterogeneity of the prepared sample. Besides, the overlapping between the different colours at their boundaries reflects the connectivity strength between the various phases.

3.2. Electrochemical and corrosion behavior of Zn and Zn–0.5Ni alloy in 7 M solution of KOH

3.2.1. Extrapolation of cathodic and anodic Tafel lines

Fig. 3 represents the experimental results from polarization curves of Zn–0.5Ni alloy at different temperatures with scan rate 1 mV s^{-1}. Corrosion parameters were calculated on the basis of cathodic and anodic potential vs. current density characteristics in the Tafel potential region [30,31]. The values of the corrosion current density (I_{corr}) for Zn and Zn–0.5Ni alloy were determined by extrapolation of the cathodic and anodic Tafel lines to corrosion potential (E_{corr}). It can be seen that a marked shift in both cathodic and anodic branches on the polarization curves towards higher current densities as an increase of temperature. This indicates that the rates of hydrogen evolution reaction and anodic dissolution increase with increasing temperature [32]. Similar trend is obtained in the case of pure Zn in the same concentration of KOH solution.

The curves of Fig. 4 show comparison between Tafel plot of both pure Zinc and its investigated alloy in 7 M KOH solution at 25 °C. It is observed that the cathodic and anodic branches shift to lower current densities in the case of alloy compared with those of pure zinc. On the other hand, the negative shift in the corrosion potential (E_{corr}) with simultaneous decrease in the corrosion rate of alloy compared with that for pure Zn can be ascribed to the

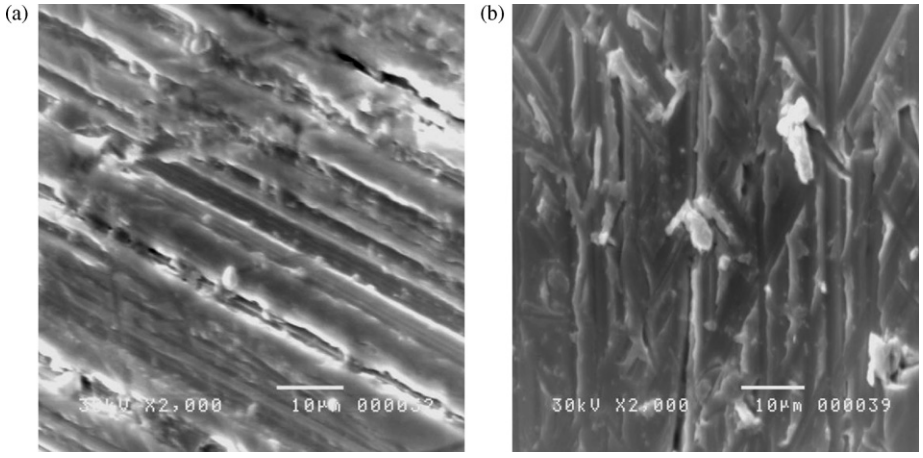

Fig. 2. SEM photographs of the surface of (a) pure Zn and (b) Zn–0.5Ni alloy at magnification 2000×.

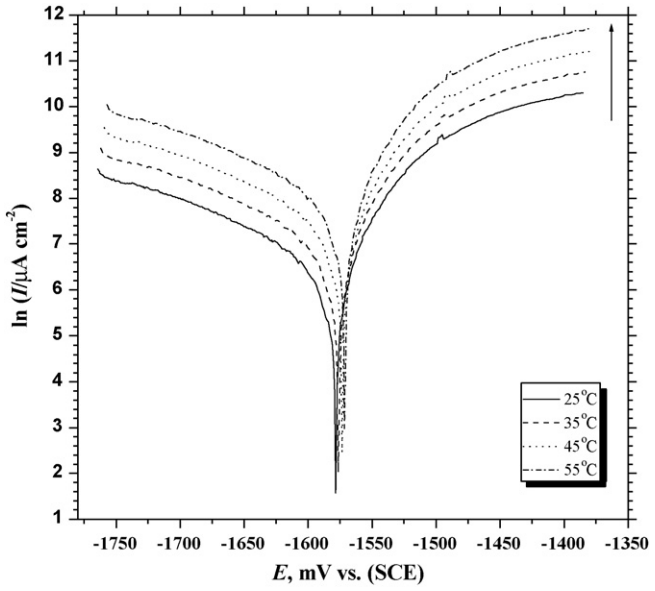

Fig. 3. Tafel polarization curves for Zn–0.5Ni alloy in 7 M solution of KOH at different temperatures.

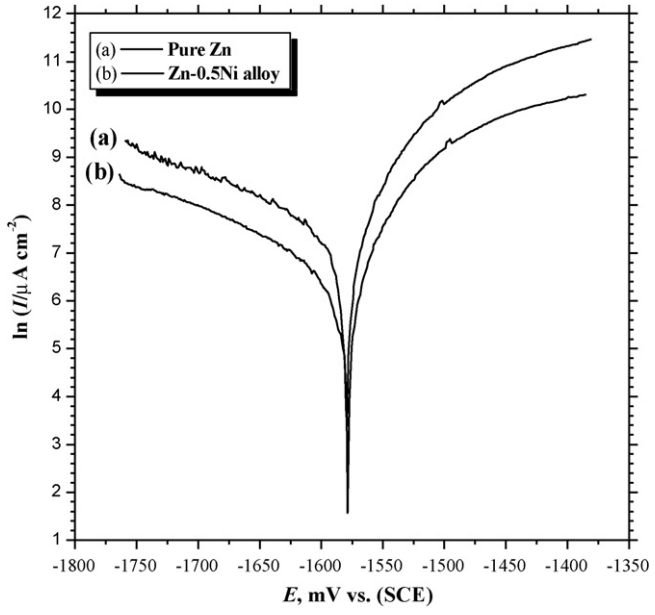

Fig. 4. Comparison between Tafel polarization curves for (a) pure Zn and (b) Zn–0.5Ni alloy in 7 M solution of KOH at 25 °C.

Table 2
Apparent activation energy (E_a) in kJ mol^{-1} of Zn and Zn–0.5Ni alloy in 7 M KOH solution.

Metal and alloy	E_a, kJ mol^{-1}
Zn	14.60
Zn–0.5Ni alloy	21.15

polarizing action of γ-Zn_3Ni phase, which is recorded using X-ray diffraction on the alloy surface. Since hydrogen overpotential on particles of γ-Zn_3Ni phase may be higher than that of pure Zn [33]. It is concluded that the presence of γ-Zn_3Ni phase in the alloy as a separated phase or in pearlitic structure acts as cathodic sites on the alloy surface. Therefore, it is assumed that the presence of Ni as a minor alloying element decreases the density of active sites on the alloy surface compared with that of zinc, and consequently the rate of soluble complex formation with the OH^- anions decreases. The results exhibited that E_{corr} value shifts to more negative potential in the case of alloy compared with that of zinc. This indicates that the changes in potential of hydrogen evolution towards more negative values have a positive effect on charge efficiency and self-discharge [34].

The polarization results (Table 1) indicate that the corrosion current density (I_{corr}) of Zn–0.5Ni alloy is 0.492 mA cm^{-2}, and for pure zinc metal 1.096 mA cm^{-2} at 25 °C. This indicates that the addition of 0.5% Ni to Zn reduces the corrosion rate by 55%. This result can be interpreted by the increasing corrosion resistance for the alloy compared to base metal [35].

The values of Tafel slopes (b_c and b_a) in Table 1 exhibited that these values of b_c and b_a in the case of alloy are higher than those of pure zinc. On the other hand, the cathodic Tafel slopes (b_c) are also found to be greater than the respective anodic Tafel slopes (b_a). These observations are correlated with the fact that the cathodic exchange-current density values are less than those of the anodic counter parts. It can be concluded that the overall kinetics of corrosion of both Zn and Zn–0.5Ni alloy in 7 M KOH solution are under cathodic control [23]. The corresponding value for the transfer coefficient (α) lies between 0.46 and 0.57, indicating that the processes correspond to a simple discharge mechanism for hydrogen evolution reaction.

The data in Table 1 show that the current density (I_{corr}) increases and corrosion potential values shift to more positive direction with increasing temperature in the case of both pure Zn and Zn–0.5Ni alloy.

Arrhenius plots for Zn and Zn–0.5Ni alloy in 7 M KOH solution are shown in Fig. 5. The activation energy can be obtained by Arrhenius equation:

$$\log I_{corr} = \log A - \frac{E_a}{2.303R}\frac{1}{T} \quad (1)$$

where T is the absolute temperature, A the prexponential constant and R the universal gas constant and E_a the apparent activation energy. The values of apparent activation energy (E_a) of Zn and its alloy for corrosion, determined from the slope of $\log I_{corr}$ vs. $1/T$

Table 1
Corrosion parameters obtained from Tafel polarization for pure Zn and Zn–0.5Ni alloy in 7 M solution of KOH at different temperatures.

Metal and alloy	Temperatures, °C	$-E_{corr}$, mV	I_{corr}, mA cm^{-2}	b_a, mV decade^{-1}	$-b_c$, mV decade^{-1}	α
Zn	25	1577	1.096	75	109	0.54
	35	1575	1.998	76	110	0.54
	45	1573	3.29	78	112	0.56
	55	1570	6.00	80	113	0.57
Zn–0.5Ni alloy	25	1581	0.492	84	127	0.46
	35	1580	0.735	86	128	0.46
	45	1579	1.48	87	130	0.47
	55	1577	2.28	88	131	0.47

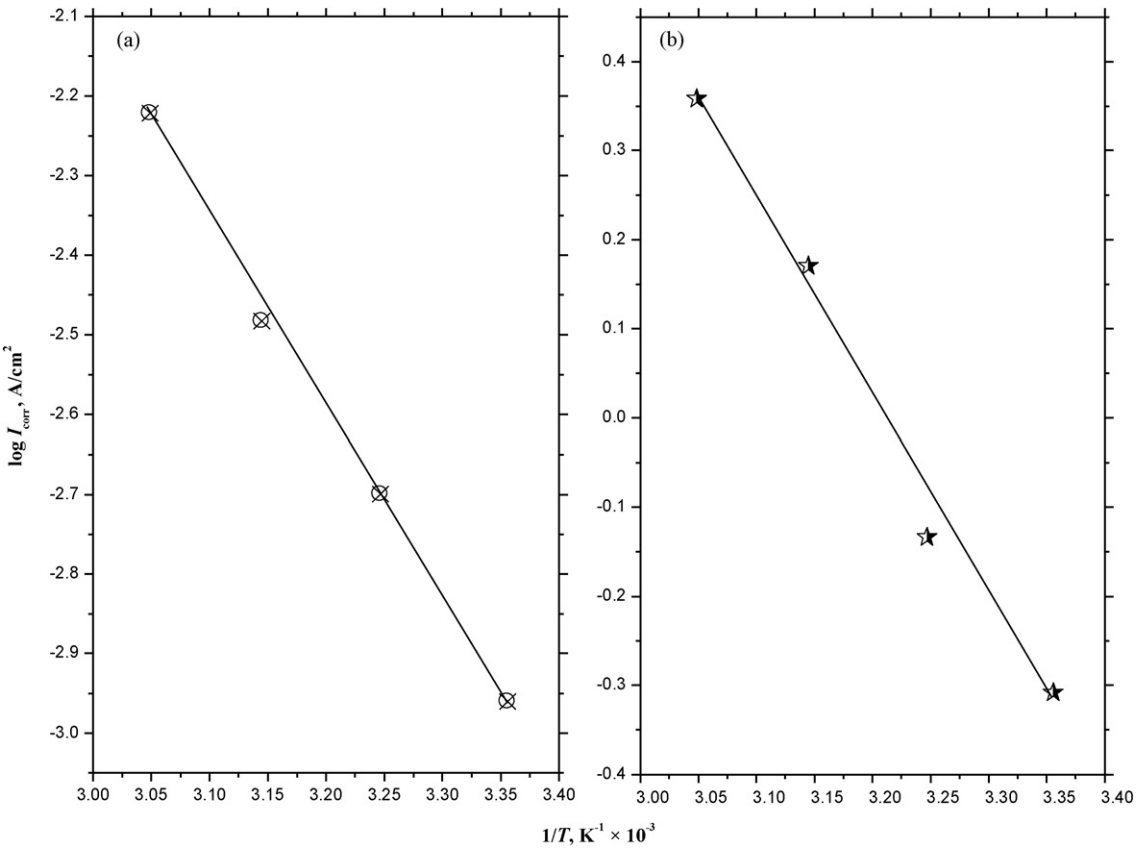

Fig. 5. Arrhenius plots for (a) pure Zn, (b) Zn–0.5Ni alloy corrosion in 7 M solution of KOH.

plots, are given in Table 2. The data show that, the value of apparent activation energy (E_a) for Zn–0.5Ni alloy in 7 M KOH solution is higher than that in the case of pure Zn. This behavior may be attributed to the presence of γ-Zn_3Ni phase which enhances the activation energy barrier of the corrosion, whereby reduces the corrosion rate [36]. The higher value of E_a in the case of Zn–0.5Ni alloy is run parallel with its lower corrosion rate. This behavior may be ascribed to the lower active sites and/or a decrease of anodic to cathodic area ratio [37]. Stevanović et al. [38] stated that the presence of the γ-phase in the deposited alloy not only makes a lower rate of the hydrogen evolution reaction, but also inhibits that at the γ-phase. It is claimed in the literature that it is such a single phase formation in the alloy which provides the best protection with the lowest self corrosion rate [39].

3.2.2. Potentiodynamic polarization curves

The curves of Fig. 6 show the potentiodynamic polarization curves for pure Zn anode in 7 M solution of KOH at different temperatures (25–55 °C) and at scan rate 1 mV s^{-1}. The polarization curves were swept from the steady state of open-circuit potential (E_{corr}) up to +1000 mV vs. SCE. The anodic polarization curves exhibit an active/passive transition. In the active region, the dissolution current increases linearly with the applied potential, then followed by the appearance of two peaks (A_I and A_{II}). The broad peak A_I is well defined at about −1390 mV vs. SCE, which can be associated with the active dissolution of Zn to Zn(II) species according to the reactions [40]:

$$Zn \rightarrow Zn^{2+} + 2e^- \quad (2)$$

and

$$Zn^{2+} + 2OH^- \rightarrow Zn(OH)_2 \quad (3)$$

While small anodic peak A_{II} appearing at about −1081 mV vs. SCE, and may be related to dehydration of $Zn(OH)_2$ to ZnO as the following reaction:

$$Zn(OH)_2 \rightarrow ZnO + H_2O \quad (4)$$

After the formation of ZnO on the electrode surface, $Zn(OH)_2$ or ZnO dissolves by the reaction with further hydroxide to form the

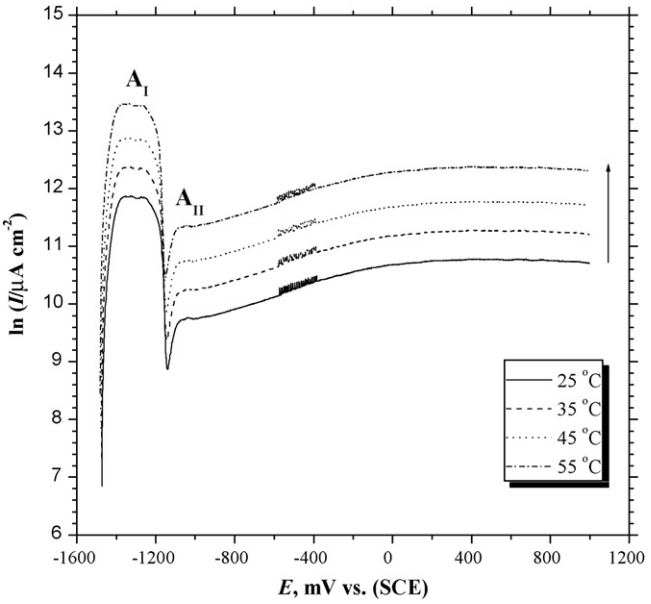

Fig. 6. Potentiodynamic anodic polarization curves for pure Zn in 7 M solution of KOH at different temperatures.

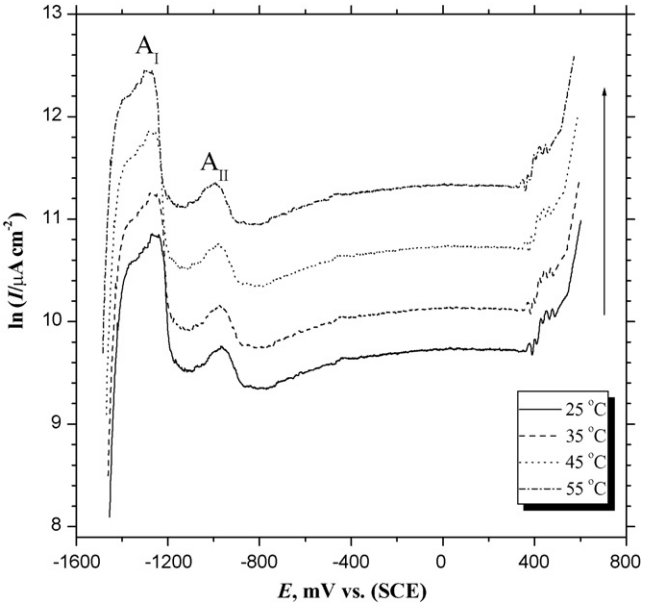

Fig. 7. Potentiodynamic anodic polarization curves for Zn–0.5Ni alloy in 7 M solution of KOH at different temperatures.

zincates ions $[Zn(OH)_4]^{2-}$ according to [41]:

$$Zn(OH)_2 + 2OH^- \rightarrow [Zn(OH)_4]^{2-} \quad (5)$$

or

$$ZnO + H_2O + 2OH^- \rightarrow [Zn(OH)_4]^{2-} \quad (6)$$

When the electrolyte in the immediate vicinity of the electrode becomes supersaturated with $[Zn(OH)_4]^{2-}$, $Zn(OH)_2$ precipitates on Zn surface to form a porous film. Dissolution proceeds according to reaction (5) or (6) until the pH within the porous film is reduced to the extent that ZnO is insoluble. At this stage, the electrode surface is passivated because of the surface formation of a thin compact ZnO layer.

The present data display that with increasing temperature, the peak current (I_p) is increased, while their corresponding peak potential (E_p) is slightly shifted to more positive value. It seems possible that the concentration of Zn^{2+} complexes increases with temperature. Accordingly, the concentration of uncomplexed Zn^{2+} decreases. This leads to an increase in the peak currents and to a positive shift in the peak potentials with a simultaneous delay in the passivation, and consequently the corrosion rate is increased [42].

Fig. 7 shows the potentiodynamic *E*/*I* curves of Zn–0.5Ni alloy in 7 M solution of KOH at different temperatures. The curves were swept from E_{ocp} up to positive potential (+1000 mV vs. SCE) with scan rate 1 mV s^{-1}. The anodic sweep exhibits an active/passive behavior. The active dissolution potential region involves two anodic peaks (A_I and A_{II}) prior to permanent passive region. The peak A_I is well defined at about −1295 mV vs. SCE which can be associated with the electro-formation of ZnO film as a result of adsorption of OH^- ion on the metal surface according to the overall reaction [43]:

$$Zn + (OH^-)_{ads} \rightarrow ZnO + H^+ + 2e^- \quad (7)$$

While the second peak A_{II} appearing at about −980 mV vs. SCE, which is related to the formation of $HNiO_2^-$ species or $Ni(OH)_2$ corresponding to the following reaction [44]:

$$Ni + 2OH^- \rightarrow [HNiO_2]^- + H^+ + 2e^- \quad (8)$$

and/or

$$Ni + 2OH^- \rightarrow Ni(OH)_2 + 2e^- \quad (9)$$

It is interest to note that $Ni(OH)_2$ is thermodynamically unstable with respect to the corresponding oxide. This suggests that dehydration of hydroxide can occur on the alloy surface during the potential sweep to positive direction as the following:

$$Ni(OH)_2 \rightarrow NiO + H_2O \quad (10)$$

When the formation of oxides (ZnO and NiO) exceeds its dissolution rate, the current drops indicating the onset of passivation due to the precipitation of ZnO and NiO on the surface which blocks the dissolution of active sites and causes inactivation of a part of the surface toward the corrosive medium [26]. The passive region extends over the passive potential range of about +400 mV vs. SCE, and the I_{pass} rises suddenly without any sign of oxygen evolution. Such behavior may have been connected to the high dissolution rate of the oxides in the concentrated KOH solution [45]. On the other hand, the increase of the current density at high positive potentials (more than +800 mV) may be due to the formation of NiOOH, which can be thermodynamically favorable and more stable according to the following reaction [46]:

$$NiO + OH^- \rightarrow NiOOH + e^- \quad (11)$$

The results also show that the peak potential $(E_p)_{AI}$ of the alloy shifts toward more positive values compared with that related to pure zinc. This behavior confirms that the tendency of the alloy towards passivity decreases as a result of the presence of a minor alloying Ni with Zn. This behavior indicates the beneficial affect of the minor Ni content (0.5% Ni) in the alloy, which delays the oxide film formation on the alloy surface. This exhibits that addition of small amount of Ni to pure Zn, improves the charge efficiency and self-anodes discharge of Zn, which can be used as anodes in the batteries. However, the oscillations observed in the polarization curves at more positive potentials in the case of alloy, can be attributed to the competition between the anodic film formation and chemical dissolution of the passive oxide film on the alloy surface in high concentrated KOH solution [37].

The data also show that, an increase in temperature enhances $(I_p)_{AI}$ and $(I_p)_{AII}$, passivation current and shifts $(E_p)_{AI}$ and $(E_p)_{AII}$ toward more positive values. The relation between E_b and temperature showed that an increase in the temperature accelerates the rate of diffusion and migration of the reactant and product species [47], and consequently the corrosion reactions are increased. Such effects of temperature on passive current of Zn–0.5Ni alloy may be attributed to an increase in solubility of oxides (ZnO and NiO) with temperature.

The values of $\log I_p$ (current peak) for various temperatures were plotted as a function of $1/T$ (K) (Arrhenius plot). The apparent activation energy for the electrochemical process associated with peak A_I for Zn and Zn–0.5Ni alloy is calculated from the slope of this Arrhenius plot. The data furnish an apparent activation energy values E_a = 17.53 and 26.12 kJ mol^{-1} for pure Zn and Zn–0.5Ni alloy, respectively.

3.2.3. Effect of scan rates

Fig. 8 represents the anodic potentiodynamic polarization curves of Zn–0.5Ni alloy in 7 M KOH at different scan rates at 25 °C. It is obvious that, the current density of peaks increases while the peaks potential shifts to more positive values with increasing the sweep rate. A linear relation is observed by plotting the peak current (I_p) vs. $\upsilon^{1/2}$. In the case of pure Zn, the line passes through the origin as shown in Fig. 9. The $\upsilon^{1/2}$ dependence observed can be interpreted on the basis of Delahay equation [48]:

$$I_p = abZ^{1/2}CD^{1/2}\upsilon^{1/2} \quad (12)$$

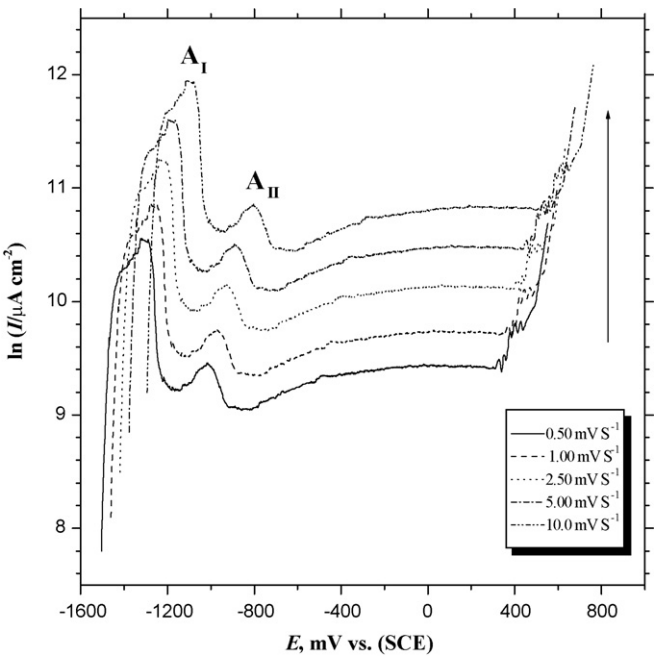

Fig. 8. Effect of different scan rates on the potentiodynamic anodic polarization of Zn–0.5 Ni alloy in 7 M KOH at 25 °C.

where a, b are constants, Z is the number of exchanged electrons, C the concentration and D the diffusion coefficient of the diffusing species and υ the scan rate. This result suggests that the dissolution of Zn is under diffusion control by mass transport into the solution. However, in the case of Zn–0.5Ni alloy the straight lines do not pass through the origin (Fig. 9). This result could be explained in terms of mixed process including diffusion controlled dissolution and direct film formation [49].

A plot of peak potential (E_p) of peak A_I in the case of pure Zn and peaks A_I and A_{II} of Zn–0.5Ni alloy vs. $\upsilon^{1/2}$ is given in Fig. 10. A linear relationship is obtained, indicating that the observed sweep rate dependence of E_p is consistent with irreversible formation of active dissolution of Zn [50].

3.2.4. Potentiostatic measurements

Fig. 11a and b shows the current-time transient curves of Zn and Zn–0.5Ni alloy in 7 M KOH solution at different applied potentials and at 25 °C. It is observed that the current density decreases with time (except in the case of Zn–0.5Ni alloy at certain positive potential) at different applied potentials. The results show clearly that the currents measured of the investigated electrodes in the examined solution at more positive potentials are significantly reduced in comparison with the currents obtained at more negative potentials. This behavior confirms that the tendency of the two mentioned electrodes towards passivity increases with shifting applied potential to more positive direction. However in the case of Zn–0.5Ni alloy, it is observed that the current density vs. time at certain positive potential (+425 mV vs. SCE) gives opposite behavior to that observed for pure Zn. That is, after certain time of immersed Zn–0.5Ni alloy in KOH solution, the current density rises suddenly. This indicates that the oxide film formed on the alloy surface tends to breakdown, and reactivation of the alloy surface takes place at certain positive potential [51]. However it is observed that the breakdown of the passive layer shifts to less positive potential with increasing temperature. We proposed that the reason why the passive film formed on the alloy surface has ability to breakdown at certain positive potential in KOH solution, as due to that some Ni(II) is precipitated in ZnO lattice [52]. Accordingly the addition of small amount from Ni to Zn increases the breakdown sensitivity of the

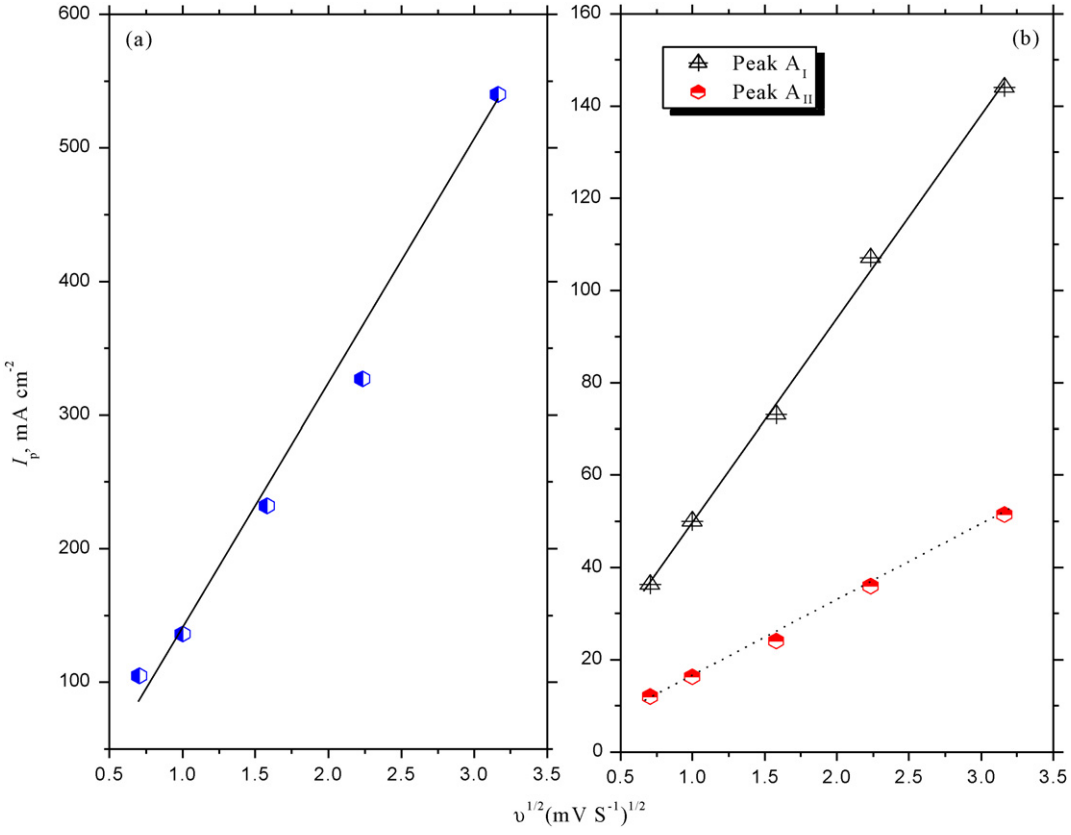

Fig. 9. The linear dependence of I_p vs. $\upsilon^{1/2}$ for (a) pure Zn and (b) Zn–0.5Ni alloy in 7 M KOH at 25 °C.

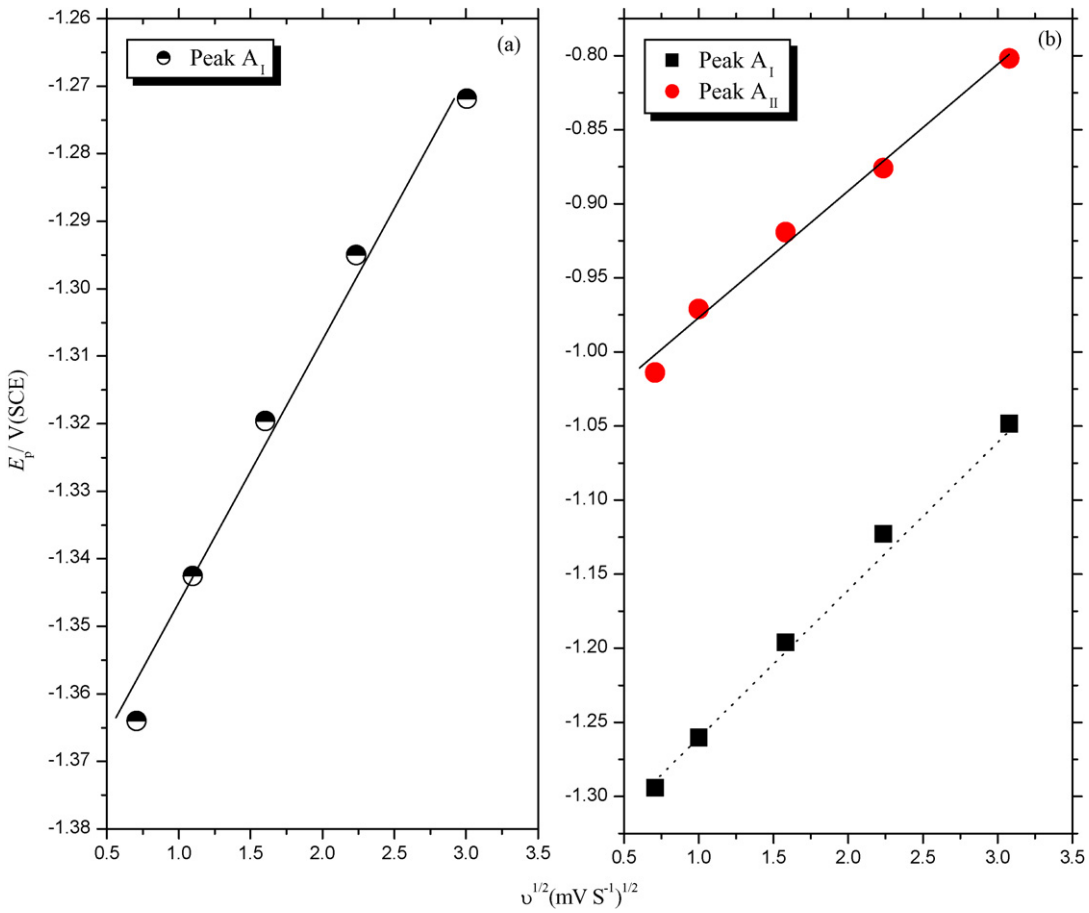

Fig. 10. Dependence of the peak potential E_p on $\upsilon^{1/2}$ for (a) pure Zn and (b) Zn–0.5Ni alloy in 7 M KOH solution at 25 °C.

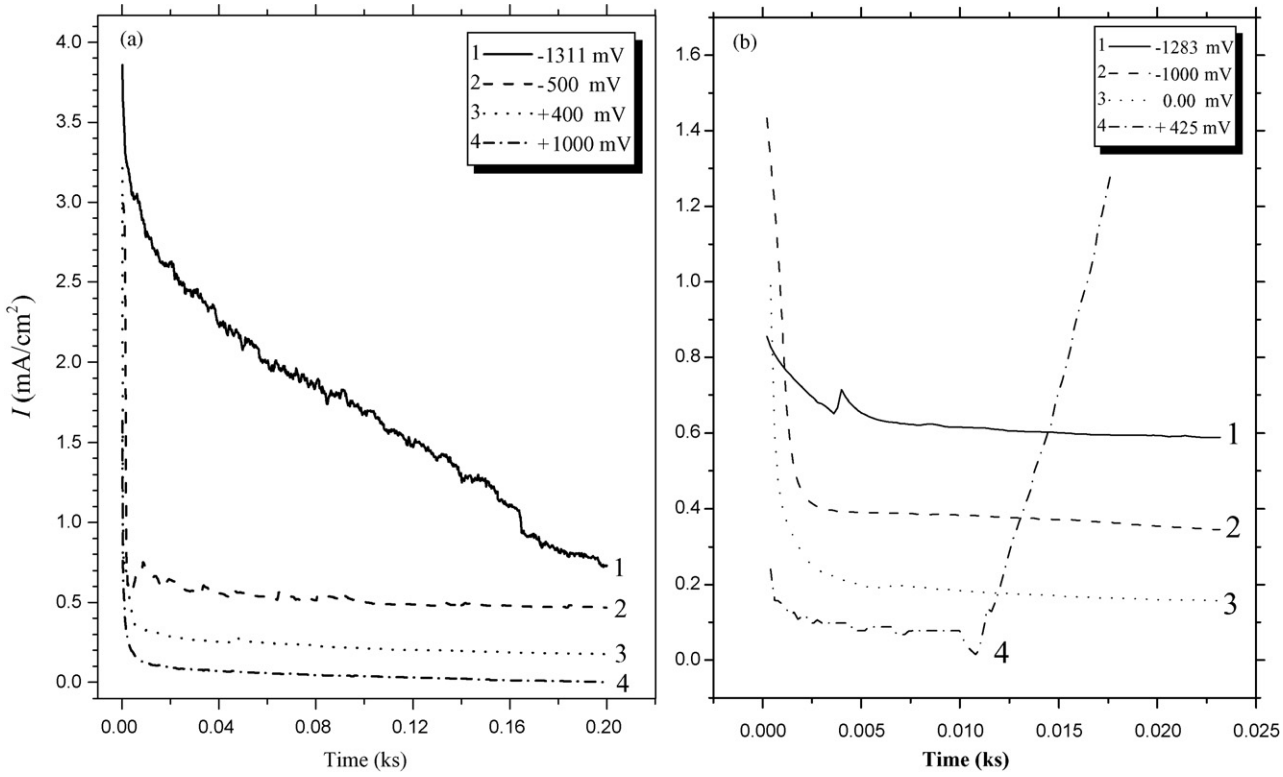

Fig. 11. Potentiostatic transient's current vs. time curves for (a) pure Zn, (b) Zn–0.5Ni alloy in 7 M KOH solution at different applied potentials.

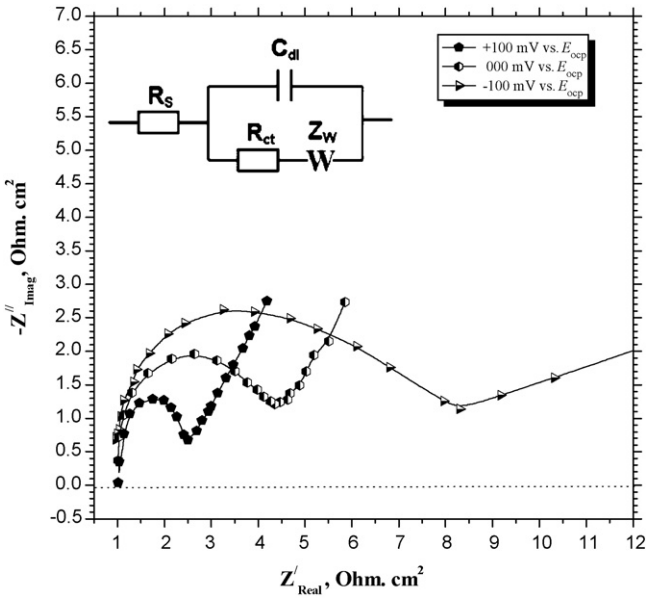

Fig. 12. Nyquist plot for pure Zn in 7 M KOH at applied different potentials, Ac amplitude 5 mV, the frequencies from 100 kHz to 5 Hz, and at 298 K. Inset (top) is the Randle's equivalent circuit.

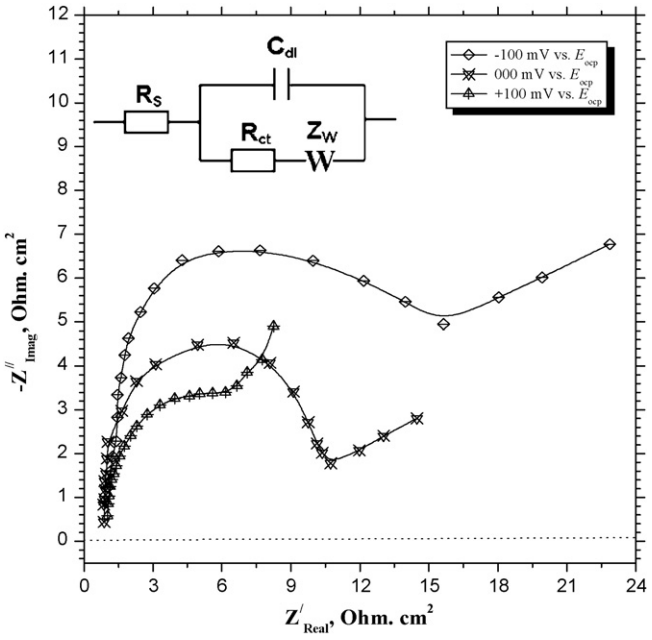

Fig. 13. Nyquist plot for Zn–0.5Ni alloy in 7 M KOH at applied different potentials, Ac amplitude 5 mV, the frequencies from 100 kHz to 5 Hz, and at 298 K. Inset (top) is the Randle's equivalent circuit.

passive layer, leading to worse anti-corrosive abilities, but better conductivity. This result supports the potentiodynamic behavior of the studied alloy at the same applied potential (+0.425 V vs. SCE).

3.2.5. Electrochemical impedance spectroscopy measurements (EIS)

The impedance for both pure Zn and Zn–0.5Ni alloy in 7 M KOH at different applied potentials values around the steady state of open-circuit potential (E_{corr}) is plotted in the complex plane as shown in Figs. 12 and 13. The potential is selected from −100 negative to +100 mV positive with respect to the E_{ocp}. An analysis of the impedance in the examined potential range was made. The data of the charge transfer resistance, R_{ct}, and the capacity of the double layer (C_{dl}) were calculated using both the Nequist and Bode plots of the impedance spectrum (Table 3). However, the Warburg impedance (Z_w) is determined from the following equations [53]:

$$Z' = \sigma \frac{1}{\omega^{1/2}} - j\frac{\sigma}{\omega^{1/2}} \quad (13)$$

$$|z'| = \sqrt{2\sigma}/\omega^{1/2} \quad (14)$$

The Warburg coefficient, σ, can be determined from the slope of the Warburg plot (the slope of real parts of Z' vs. $1/\omega^{1/2}$; $\omega = 2\pi F$), or by fitting to an equivalent circuit model which includes a Warburg impedance. However, most equivalent circuit modeling programs return "Z_w" rather than σ, Z_w is the Warburg impedance ($Z_w = W$) which are calculating from the following equation (Table 3):

$$\sigma = \frac{1}{Z_w\sqrt{2}} \quad (15)$$

The recorded spectra show one capacitive loop at the higher frequency range (HF) followed by the Warburg Tail at lower frequency values (LF) (Figs. 12 and 13). The curves in Figs. 12 and 13 exhibit that Z_w is the Warburg impedance, related to the diffusion of soluble species from the electrode surface to the bulk of solution [54,55]. The diameter of the capacitive loop (R_{ct}) and Warburg impedance (Z_w) decrease while the capacity of the double layer (C_{dl}) increases with increasing potential in the positive direction (Table 3). This process may be argued to the corrosion process, i.e. hydrogen evolution and dissolution of Zn or Zn–0.5Ni alloy as discussed above in both Tafel plot and potentiodynamic investigations.

The equivalent circuit model used to fit the experimental data is shown inside Figs. 12 and 13 as previously reported [56]. The measured complex-plane impedance plot is similar to that calculated by the equivalent circuit model. The charge transfer resistance (R_{ct}), the Warburg impedance (Z_w) and the capacity of the double layer (C_{dl}) are determined by analysis of the complex-plane impedance plot and the equivalent circuit model. From the data obtained in Table 3, one can conclude that the higher values of both R_{ct}, Z_w and lower C_{dl} values for Zn–0.5Ni alloy compared with those of pure Zn can be attributed to the presence of Ni in Zn matrix leading to relative decrease of corrosion rate, and this behavior is in good agreement with that obtained of the Tafel plot measurements. The first conclusion, which could be extracted from these plots, is that the spectra presented show at least two time constants. The first time constant, recorded at higher frequency, where the properties of a electrode/electrolyte interface are particularly reflected, is displayed as a depressed incomplete semicircle. The electrical-equivalent-circuit (EEC) parameters, describing the process included in this time constant are R_{ct} and C_{dl}. The second time constant, depicted at lower frequencies, corresponds to a straight line (Figs. 12 and 13). This linear dependence between the imaginary and real part of the capacitance is related to the diffusion process of the soluble species, while is called Warburg impedance. Therefore, EEC parameters describing the process included in the second time constant clearly indicates the diffusion control of the soluble species.

Fig. 14 is a complex-plane impedance diagram for Zn and Zn–0.5Ni alloy in 7 M KOH solution in the passive region (at +1500 mV vs. SCE) at 25 °C. The data exhibited that a semicircle is observed at the higher frequency and the Warburg Tail at low frequency is disappeared. This result means that the impedance has become capacitive. The semicircle diameter increases in the passivation potential region more than that in the active regions. This result indicates that the charge transfer resistance (R_{ct}) is increased due to the formation of passive layer from ZnO or ZnO/NiO film in the case of both pure Zn and Zn–0.5Ni alloy, respectively. On the other hand, the disappear of Warburg Tail at low frequency with

Table 3
Impedance parameters obtained for the corrosion of pure Zn and Zn–0.5Ni alloy in 7 M solution of KOH at different applied potentials and at 25 °C.

Metal and alloy	−100 mV vs. E_{ocp}			0.0 mV vs. E_{ocp}			+100 mV vs. E_{ocp}		
	R_{ct}, Ω cm^2	C_{dl}, mF cm^{-2}	Z_w, Ω^{-1} s$^{1/2}$ cm^{-2}	R_{ct}, Ω cm^2	C_{dl}, mF cm^{-2}	Z_w, Ω^{-1} s$^{1/2}$ cm^{-2}	R_{ct}, Ω cm^2	C_{dl}, mF cm^{-2}	Z_w, Ω^{-1} s$^{1/2}$ cm^{-2}
Zn	9.5	19.0	58.2	6.0	31.0	32.3	2.50	63.0	18.6
Zn–0.5Ni alloy	21.5	3.90	115.3	12.5	10	79.5	10.60	50.0	44.2

increasing the applied potential in the positive direction (by comparison of Figs. 12 and 13 with Fig. 14) means that the diffusion species is strongly reduced. Therefore all the spectra show semicircle behavior in the passive region, quite characteristic for the pure kinetically controlled reaction [57].

The results also show that the capacitive loop in the case of Zn–0.5Ni alloy is higher compared with that of pure Zn in the passive region (Fig. 14). This behavior may be due to the presence of Ni as a minor element in the alloy, leads to changing the kinetics of ion electron transportation. This confirms that ion transportation through the passive layer is the controlling step of the corrosion process in the case of the investigated alloy [52]. It is worthy noting that the same trend is observed in the case of both pure Zn and its alloy as manifested in the same order as that obtained from potentiodynamic polarization measurements. Finally, one can conclude that the introduction of small amount of Ni into Zn can be considered as important criteria for a good battery anode, due to its high negative open-circuit potential and less corrosion rate compared with those of pure Zn.

3.2.6. Composition and properties of anodic passive film

3.2.6.1. X-ray diffraction. The composition of the passive film formed on the surfaces of Zn and Zn–0.5Ni alloy after anodic potentiostatic polarization treatment in 7 M KOH solution for 20 min at different formation potentials was examined. The passive electrode was withdrawn carefully, washed with doubly distilled water, dried, and finally examined by X-ray diffraction. Fig. 15 represents X-ray diffraction of passive film formed at peak potential of Zn electrode (−1390 mV vs. SCE) in 7 M KOH. The data confirm the existence of Zn as a major, but $Zn(OH)_2$ and ZnO as a minor constituents. These results indicate that the peak potential of zinc in KOH solution is related to the formation of $Zn(OH)_2$/ZnO system on the electrode surface. While the data obtained for zinc electrode treated at +1000 mV vs. SCE (passive region) exhibited that the surface contains ZnO only. In addition, there are not any data of XRD related to the presence of Zn metal in this region. This provides that Zn surface is completely covered by a thick oxide film of ZnO. This trend may be attributed to the direct oxidation of Zn to ZnO in the passive region.

The data in Fig. 16 for the Zn–0.5Ni alloy treated potentiostatically at −1.295 V vs. SCE (peak A_I) in 7 M KOH solution at 25 °C reveal that the surface contains Zn, γ-Zn_3Ni, and small amounts of ZnO. This confirms that the peak potential at −1295 mV vs. SCE may be attributed to ZnO formation on the alloy surface. However, the data of the same alloy, treated at −980 mV vs. SCE (peak A_{II}), show that the surface contains large amounts of Zn and small amounts of $Ni(OH)_2$/NiO system and traces from ZnO. Accordingly, the data reveal that the peak potential (peak A_{II}) of Zn–0.5Ni alloy is related to the formation of $Ni(OH)_2$/NiO and ZnO on the electrode surface. These results support our suggestion that the investigated peak potential (A_{II}) is related to the formation of $Ni(OH)_2$/NiO on the

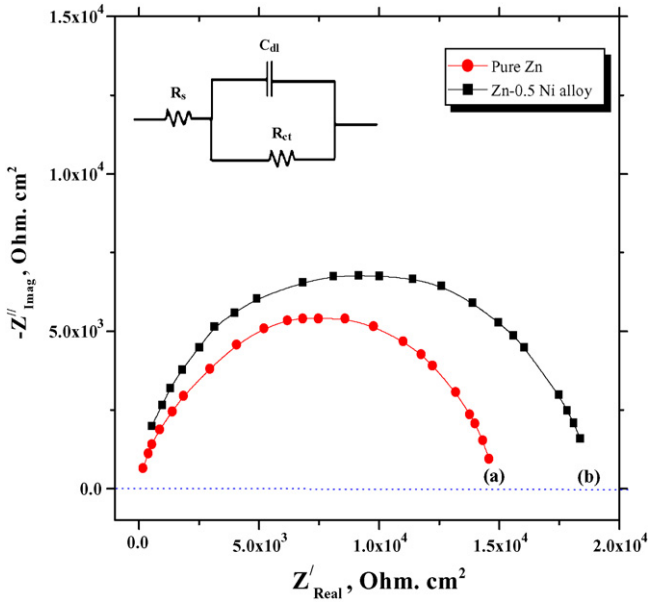

Fig. 14. Nyquist plot for oxide film formed anodically at +1500 mV vs. SCE on (a) pure Zn and (b) Zn–0.5Ni alloy in 7 M KOH at E_{ocp}, Ac amplitude 5 mV, the frequencies from 100 kHz to 5 Hz, and at 298 K. Inset (top) is the equivalent circuit.

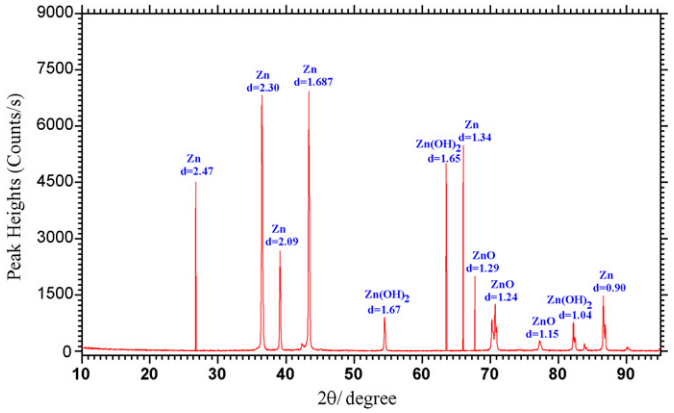

Fig. 15. X-ray diffraction analysis for the passive film on Zn electrode surface formed anodically in 7 M solution of KOH at applied potential −1.39 V (SCE) and 25 °C.

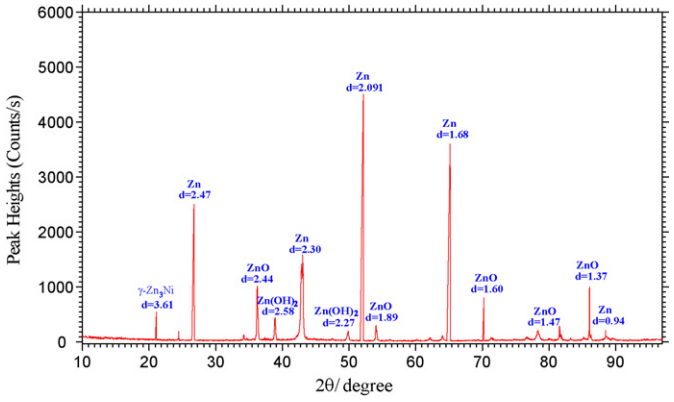

Fig. 16. X-ray diffraction analysis for the passive film on Zn–0.5Ni alloy surface formed anodically in 7 M solution of KOH at applied potential −1.295 V (SCE) (peak A_I) and 25 °C.

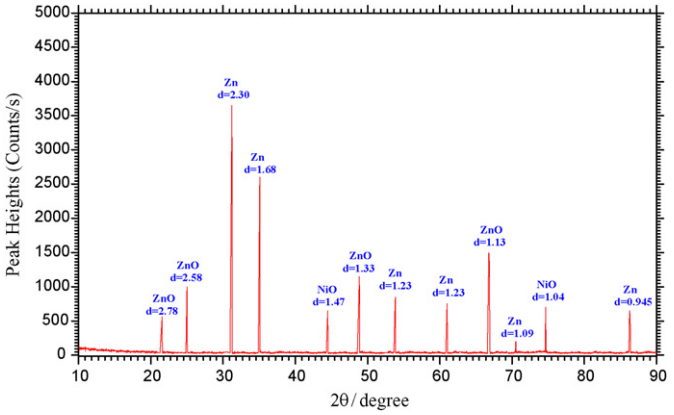

Fig. 17. X-ray diffraction analysis for the passive film on Zn–0.5Ni alloy surface formed anodically in 7 M solution of KOH at applied potential +0.425 V (SCE) and 25 °C.

electrode surface. The data for the same Zn–0.5Ni alloy treated at +100 mV vs. SCE (passive region) reveal that the surface is covered by ZnO as a major and NiO as a minor constituent. Fig. 17 shows XRD data of Zn–0.5Ni alloy treated at +425 mV vs. SCE (at breakdown potential of oxide layer). The data infer that the surface contains Zn and small amounts of ZnO and NiO. Comparison between X-ray data for the presence of ZnO and NiO amounts on the surface of the alloy at both +100 mV (less positive potential) and +425 mV (more positive potential), reveal that large amounts of ZnO and NiO is formed at less positive potential compared with those amounts formed at more positive potential. This provides that at more positive potential, the most of ZnO and NiO dissolve in KOH solution and leads to reactivation of the electrode surface. Therefore, XRD results are in good agreement with both potentiodynamic and potentiostatic measurements, which the current density increases suddenly at the investigated potential (+425 mV vs. SCE).

3.2.6.2. Microscopic examination. Fig. 18a and b shows the micrographs of the anodic passive film formed potentiostatically on surface of Zn in 7 M solution of KOH at applied potentials −1300 (peak A_I) and +1000 mV vs. SCE (passive region) with a magnification of 1000×. It may appear from Fig. 18a that the surface is almost completely covered by thick porous layer of corrosion product and loosely bound to the metal surface. The crystals of this layer exhibit different shapes that may be related to a mixture of $Zn(OH)_2$ or ZnO. However, the photograph of Zn treated anodically at +1000 mV vs. SCE (passive region) given in Fig. 18b, recognized that the crystal size is smaller and greater than that at more negative potential (peak A_I). The crystals of the layer become more adhered on the surface, and are not compact, i.e., there are vacancies between them. Therefore, SEM results support the potentiodynamic measurements that high current density in the passive region is obtained. This behavior may be due to an amount from this layer dissolved in the bulk of solution.

Fig. 19a–d shows the micrographs of the anodic passive film formed potentiostatically on surface of Zn–0.5Ni alloy in 7 M solution of KOH at applied potentials −1290, −984, +100 and +425 mV vs. SCE with a magnification of 1000×. It would be recognized from Fig. 19a that the treated surface at −1290 mV (peak A_I) is partially covered by the passive layer, so that the electrode surface can be seen. One layer is observed on the electrode surface, and its crystals exhibit different shapes compared with those of pure zinc (peak A_I). This indicates that the presence of Ni in the alloy as a minor alloying element retards the formation of $Zn(OH)_2$ or ZnO on the alloy surface, and the layer may be related to ZnO. However, the higher corrosion resistance of the alloy leads to lower current density of peak A_I than that of pure Zn. Fig. 19b shows SEM photographs of Zn–0.5Ni alloy treated at −984 mV vs. SCE (peak A_{II}). It is found that the surface is almost completely covered by adhered passive oxides. Two layers are observed on the electrode surface. The crystals of the upper layer exhibit different shapes, and the surface is partially covered by bigger crystals compared with those observed in Fig. 19a. The second layer seems to lie below the upper layer and their crystals sizes are smaller. These observations are in agreement with the data of X-ray diffraction that, the upper layer is related to ZnO, while the underneath layer is due to $Ni(OH)_2$ or NiO formation. For the electrode surface treated anodically at +100 mV vs. SCE (more positive potential; Fig. 19c), it appears two layers of the oxide crystals on the alloy surface (double nature). It is observed that the amount of the crystals at the upper layer decreases and becomes more distant apart than those in Fig. 19b, the quantity of the oxide crystals in the underneath layer increases with smaller size. Whereas the crystals of the upper layer become loosely bound to the alloy surface, and an amount from this layer dissolves in the bulk of the solution. In addition the crystals of the underneath layer are distorted. This observation may be attributed to the partially dissolving ability of OH^- ions on the crystals of the oxide film. Fig. 19d shows SEM photographs of Zn–0.5Ni alloy treated at +425 mV vs. SCE (at the breakdown potential of oxide layer). The data show that the oxide film formed on the alloy surface is less than that formed at less positive potential (Fig. 19c). Thus some parts of the alloy surface can be seen. Therefore, SEM results are in good agreement with both potentiodynamic and potentiostatic

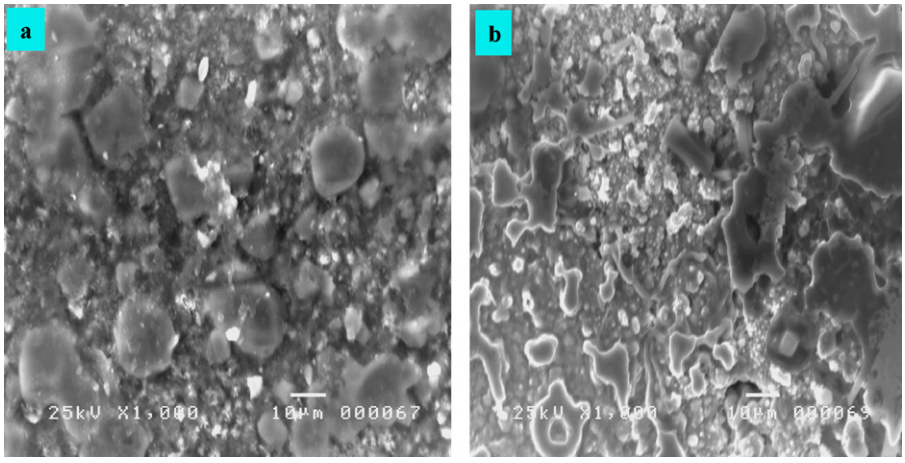

Fig. 18. SEM photographs of passive film on the Zn surface formed anodically in 7 M KOH solution at (a) −1300 mV and (b) +1000 mV at magnification.

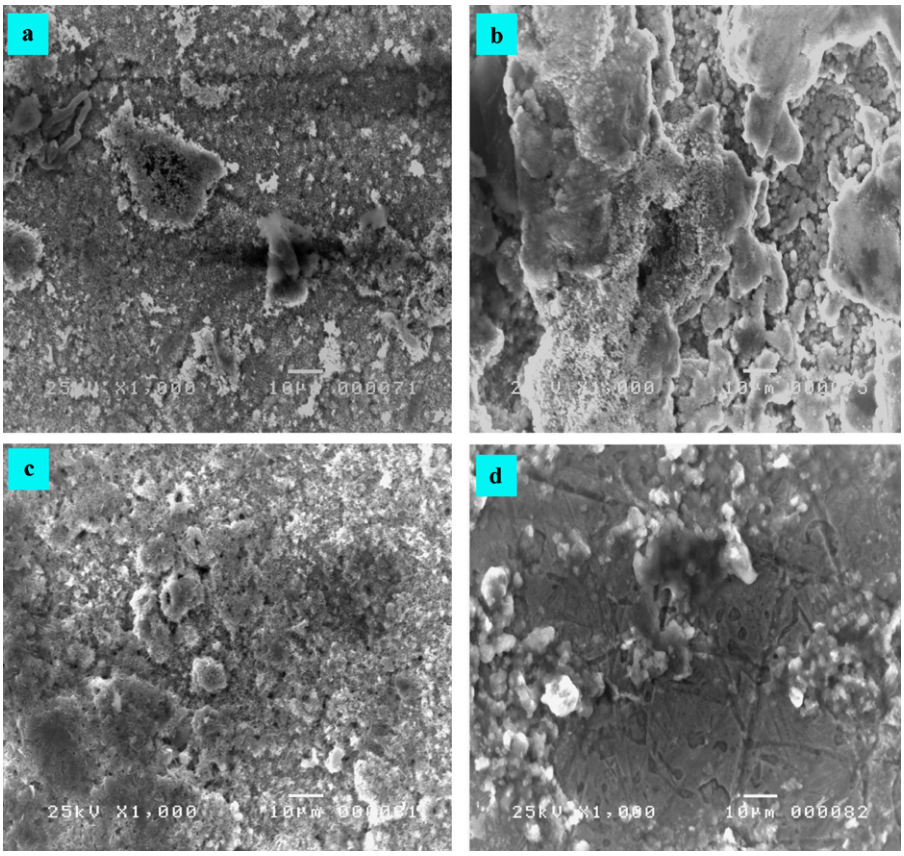

Fig. 19. SEM photographs of passive film on the Zn–0.5Ni alloy surface formed anodically in 7 M KOH solution at (a) −1290 mV, (b) −984 mV, (c) +100 and (d) +425 mV at magnification 1000×.

measurements, which the current density increases suddenly at the investigated potential (+425 mV vs. SCE).

4. Summary

In this paper, the effect of minor nickel alloying with zinc on the corrosion resistance of zinc in strong alkaline solution was investigated by different techniques. Several conclusions can be withdrawn from this investigation:

1. Generally, Zn–0.5Ni alloy (0.5% Ni) exhibited good anti-corrosive properties in strong alkaline solution compared with those of pure zinc.
2. The data of Tafel plot extrapolation showed that the cathodic and anodic branches shift to lower current densities on the alloy surface compared with those of pure zinc. Moreover negative shift in corrosion potential (E_{corr}) with simultaneous decrease in the corrosion rate of the alloy compared with those of pure zinc are obtained.
3. The potentiodynamic potential–current density curves displayed two anodic peaks of both pure zinc and Zn–0.5Ni alloy in the investigated alkaline solution. In the case of pure zinc, the two peaks may be corresponding to the formation of $Zn(OH)_2$ and ZnO, respectively. While the two peaks in the case of the alloy may be related to ZnO and NiO, respectively. The results showed that the peak current (I_{AI}) is lower in the case of alloy compared with that of pure zinc. This indicates that the presence of Ni as a minor alloying element with zinc decreases the anodic dissolution current of the alloy, and hence improves its stability against corrosion.
4. Potentiodynamic data are found to be in good agreement with the Potentiostatic results that in the case of the investigated alloy, the current density rises suddenly at a certain positive potential (+425 mV vs. SCE). This indicates that the oxide film formed on the alloy surface tends to breakdown, and leading to reactivate of the alloy surface. This behavior may be attributed to the precipitation of some Ni(II) in ZnO lattice, consequently, OH^- ions have ability to dissolve those oxide particles on the alloy surface. X-ray data infer that the surface of the alloy contains small amounts of ZnO and NiO at this breakdown potential (+425 mV).
5. The active dissolution of both zinc and its alloy increases with increasing both temperature and scan rate of the two studied electrodes. The activation energy (E_a) values of the pure zinc and its alloy at both active region and peak current (I_{AI}) are calculated and compared.
6. The data obtained from electrochemical impedance spectroscopy (EIS) assumes that, the charge transfer resistance (R_{ct}) is higher and the capacity of the double layer (C_{dl}) value is lower for Zn–0.5Ni alloy compared with those of pure zinc. This behavior is in good agreement with that obtained from Tafel plot measurements.

References

[1] K.V. Kordesch, Batteries, vol. 1, Marcel Dekker, New York, 1974, p. 324.
[2] T.D. Dirkse, R. Timmer, J. Electrochem. Soc. 116 (1969) 162.
[3] M. Meeus, Y. Strauven, L. Groothhaert, Extended Abstracts 15th International Power Sources Symposium, 1986, p. 1.
[4] L.Z. Vorkapic, D.M. Drazic, A.R. Despic, J. Electrochem. Soc. 121 (1974) 1385.
[5] M. Takahashi, Research Report for Zinc Electrode in Alkaline Solution (1985), The Electrochemical Society of Japan, 1986, p. 1.
[6] M. Yano, M. Nogami, I. Yonezu, K. Nishio, Y. Akai, M. Kurimura, Denki Kagaku 65 (1997) 154.

[7] M. Yano, Y. Akai, M. Kurimura, S. Fujitani, K. Nishio, Denki Kagaku 65 (1997) 650.
[8] M. Yano, Y. Akai, M. Kurimura, S. Fujitani, K. Nishio, J. Power Sources 74 (1998) 129.
[9] A. Miura, K. Takada, R. Okazaki, H. Ogawa, T. Uemura, Y. Nakamura, N. Kasahara, Denki Kagaku 57 (1989) 459.
[10] A. Miura, K. Takada, R. Okazaki, H. Ogawa, T. Uemura, Y. Nakamura, N. Kasahara, Extended Abstracts 55th Electrochemical Society of Japan, 1988, p. 16.
[11] A. Miura, Extended Abstracts Third Colloidal and Surface Chemistry Symposium in Japan, 1996, p. 66.
[12] K. Yamakawa, H. Tsubakino, K. Kawanishi, Denki Kagaku 59 (1991) 325.
[13] N. Kasahara, T. Uemura, A. Okada, Extended Abstracts 27th Battery Symposium in Japan, 1986, p. 7.
[14] T. Yamasoto, T. Uemura, M. Nakamura, N. Kasahara, A. Miura, K. Takada, R. Okazaki, H. Ogawa, Extended Abstracts 28th Battery Symposium in Japan, 1987, p. 37.
[15] F.R. McLarnon, E.J. Cairns, J. Electrochem. Soc. 138 (1991) 645.
[16] K.A. Striebel, F.R. McLarnon, E.J. Cairns, J. Power Sources 47 (1994) 1.
[17] J. Dobryszycki, S. Biallozor, Corros. Sci. 43 (2001) 1309.
[18] M. Paramasivam, S. Venkatakrishna Iyer, V. Kapali, Br. Corros. J. 29 (1994) 207.
[19] M. Yano, S. Fujitani, K. Nishio, Y. Akai, M. Kurimura, J. Appl. Electrochem. 28 (1998) 1221.
[20] D. Dobryszycky, S. Biallozor, Corros. Sci. 43 (2001) 1309.
[21] Y. Ein-Eli, M. Auinat, D. Starosvetsky, J. Power Sources 114 (2003) 330.
[22] Y. Sato, M. Takahashi, H. Asakura, T. Yoshida, K. Tada, K. Kobayakawa, J. Power Sources 38 (1992) 317.
[23] A.R. Suresh Kannan, S. Muralidharan, K.B. Sarangapani, V. Balaramachandran, V. Kapali, J. Power Sources 57 (1995) 93.
[24] U. Kohler, C. Antonius, P. Bauerlein, J. Power Sources 127 (2004) 45.
[25] A. El-Sayed, A.M. Shaker, H. Gad El-Kareem, Bull. Chem. Soc. Jpn. 76 (2003) 1527.
[26] S.S. Abd El Rehim, H.H. Hassan, N.F. Mohamed, Corros. Sci. 46 (2004) 1071.
[27] B.F. Giannetti, P.T. Sumodjo, T. Rabockai, J. Appl. Electrochem. 20 (1990) 672.
[28] H.S. Kim, K.H. Lee, M.C. Shin, Scr. Mater. 38 (1998) 1549.
[29] A.M. Alfantazi, U. Erb, Mater. Sci. Eng. 22 (1996) 123.
[30] R. Tremont, H. De Jesus-Cardona, J. Garcia-Orozco, R.J. Castro, C.R. Cabrera, J. Appl. Electrochem. 30 (2000) 737.
[31] J.W. Schultze, K. Wippermann, Electrochim. Acta 32 (1987) 823.
[32] L. Dezhi, P.C. Paul, L. Changqing, Corros. Sci. 50 (2008) 995.
[33] H.J. Cleary, N.D. Greene, Corros. Sci. 7 (1967) 821.
[34] B.O. Andersson, L. Ojefors, J. Electrochem. Soc. 123 (1976) 824.
[35] S.A.M. Refaey, F. Taha, T.H.A. Hasanin, Electrochim. Acta 51 (2006) 2942.
[36] A. El-Sayed, A.M. Shaker, H.M. Abd El-Lateef, Corros. Sci. 52 (2010) 72.
[37] H.S. Mohran, A. El-Sayed, H.M. Abd El-Lateef, J. Solid State Electrochem. 13 (2009) 1279.
[38] J. Stevanović, S. Gojković, M. Obradović, A. Despić, V. Nakić, Electrochim. Acta 43 (1998) 705.
[39] R. Nuomi, H. Nagasaki, Y. Foboh, A. Shibya, SAE Techn. Paper MO. 820332, Presented in Detroit, MI, 1982.
[40] M.A. Amin, Electrochim. Acta 50 (2005) 1265.
[41] R. Gus, F. Winberg, D. Tromans, Corrosion 51 (1995) 356.
[42] A. El-Sayed, F.H. Assaf, S.S. Abd El-Rehim, Hung. J. Ind. Chem. 19 (1991) 207.
[43] S.S. Abd El-Rehim, F.H. Assaf, A. El-Sayed, A.M. Zaky, Br. Corros. J. 30 (1995) 297.
[44] R. Nishimura, Corros. NACE 43 (1987) 486.
[45] E.E. Abd El Aal, Corrosion 55 (1999) 582.
[46] E.E. Abd El Aal, Corros. Sci. 45 (2003) 759.
[47] E.E. Foad, El. Sherbini, S.S. Abd El-Rehim, Corros. Sci. 42 (2000) 785.
[48] P. Delahay, Electrochemistry, Interscience Publ., New York, 1954.
[49] E.E. Foad El-Sherbini, S.M. Abd-El-Wahab, M.A. Amin, M.A. Deyab, Corros. Sci. 48 (2006) 1885.
[50] S.S.A. Rehim, S.M. Sayyah, M.M.E. Deeb, Mater. Chem. Phys. 80 (2003) 696.
[51] H.H. Hassan, S.S. Abd El Rehim, N.F. Mohamed, Corros. Sci. 44 (2002) 37.
[52] J. Xu, X. Liu, X. Li, E. Barbero, C. Dong, J. Power Sources 155 (2006) 420.
[53] Bard, Faulkner, Electrochemical Methods, Fundamentals and Applications, Wiley, 2000.
[54] O.E. Barcia, O.R. Mattos, N. pebere, B. Tribollet, J. Electrochem. Soc. 40 (1993) 2825.
[55] C. Deslouis, B. Tribollet, G. Mengoli, M. Musiani, J. Appl. Electrochem. 18 (1988) 374.
[56] K.F. Khaled, Electrochim. Acta 53 (2008) 3484.
[57] M. Metikos-Hukovic, S. Omanovic, J. Electroanal. Chem. 455 (1998) 181.